

Two-fluid numerical model of chromospheric heating and plasma outflows in a quiet-Sun

K. Murawski^{1*}, Z.E. Musielak^{2,3}, S. Poedts^{4,1}, A.K. Srivastava⁵ and L. Kadowaki¹

^{1*}Institute of Physics, University of Maria Curie-Skłodowska, Pl. Marii Curie-Skłodowskiej 5, 20-031 Lublin, Poland.

²Department of Physics, University of Texas at Arlington, Arlington, TX 7601, USA.

³ Leibniz-Institut für Sonnenphysik (KIS), Schoeneckstr. 6, 79104 Freiburg, Germany.

⁴ Centre for mathematical Plasma-Astrophysics, Department of Mathematics, KU Leuven, Celestijnenlaan 200B, 3001 Leuven, Belgium.

⁵ Department of Physic, Indian Institute of Technology (BHU), Varanasi-221005, India.

*Corresponding author(s). E-mail(s): kris.murawski@gmail.com;
 Contributing authors: zmusielak@uta.edu;
stefaan.poedts@kuleuven.be; asrivastava.app@itbhu.ac.in;
lkadowaki.astro@gmail.com;

Abstract

Purpose: This paper addresses long-standing solar physics problems, namely, the heating of the solar chromosphere and the origin of the solar wind. Our aim is to reveal the related mechanisms behind chromospheric heating and plasma outflows in a quiet-Sun. **Methods:** The approach is based on a two-fluid numerical model that accounts for thermal non-equilibrium (ionization/recombination), non-adiabatic and non-ideal dynamics of protons+electrons and hydrogen atoms. The model is applied to numerically simulate the propagation and dissipation of granulation-generated waves in the chromosphere and plasma flows inside a quiet region. **Results:** The obtained results demonstrate

that collisions between protons+electrons and hydrogen atoms supplemented by plasma viscosity, magnetic resistivity, and recombination lead to thermal energy release, which compensates radiative and thermal losses in the chromosphere, and sustains the atmosphere with vertical profiles of averaged temperature and periods of generated waves that are consistent with recent observational data. **Conclusion:** Our model conjectures a most robust and global physical picture of granulation generated wave motions, plasma flows, and subsequent heating, which form and dynamically couple the various layers of the solar atmosphere.

Keywords: Methods: numerical – Sun: atmosphere – Sun: activity

1 Introduction

One of the major, long-standing problems of solar physics concerns the source of the thermal energy required to heat the different layers of the atmosphere. Observations show that the atmosphere, with the more than one million Kelvin hot solar corona, efficiently radiates its energy and thus it must be heated to be maintained in its quasi-stationary state. For decades, different heating mechanisms were proposed but so far no common agreement regarding a complete quantitative and qualitative picture has been reached. In other words, the main physical process(es) underlying this heating of the different atmospheric layers still remains unknown. Space-borne and ground-based observational data stimulated various plausible explanations for this heating problem, among which a wave generation and dissipation mechanism is promising, especially for the chromosphere. The latter mechanism is based on thermal energy deposition essentially by compressible waves. Such compressible waves are generated by turbulent motions occurring in the solar convective zone and by granular motions in the photosphere, since both regions are vast reservoirs of mechanical energy that can be converted into wave motions.

The role of compressible (acoustic) waves in the solar chromospheric heating problem was first recognized by [Biermann \(1946\)](#) and [Schwarzschild \(1948\)](#). Contemporary high-resolution observations revealed with unprecedented spatial and temporal resolution that the presence of different types of waves and flows constitutes an integral part of the solar atmosphere (e.g., [Dadashi et al. 2011](#); [De Moortel & Nakariakov 2012](#); [Hansteen et al. 2010](#); [Kayshap et al. 2015, 2020](#); [Srivastava et al. 2017](#); [Tian et al. 2021, 2011](#)). The excitation and propagation of magneto-acoustic waves driven by the granulation have been investigated by many authors (e.g., [Hansteen et al. 2006](#); [Hegglund et al. 2011](#)). Additionally, [Hansteen et al. \(2010\)](#) and [Finley et al. \(2022\)](#) showed that the transition region and coronal heating results from the buffeting of the magnetic field lines by turbulent motions in the photosphere and in the convection zone as well as from the injection of emerging magnetic flux.

The dissipation process is more difficult to address, but multiple works (e.g., [Martínez-Sykora et al. 2017](#); [Snow & Hillier 2021](#); [Wang et al. 2021](#)) studied the wave dissipation by the shock wave and/or non-ideal MHD effects, including ion-neutral collisions. Specifically, [Martínez-Sykora et al. \(2017\)](#) studied the excitation of solar spicules by the solar granulation and their 2.5-dimensional (2.5D) model developed within the framework of radiative magnetohydrodynamics (MHD) considered a partially-ionized solar plasma and modelled its neutrals by ambipolar diffusion. In two other more recent studies, [Fleck et al. \(2021\)](#) performed numerical simulations of acoustic-gravity waves that were excited by the solar granulation, and [Snow & Hillier \(2021\)](#) used a two-fluid model to investigate the role of slow shocks in the solar atmosphere but without taking into account the solar granulation. In the approach presented in this paper, we develop a two-fluid 2.5D numerical model that accounts for interaction of protons with hydrogen atoms, and includes radiative loss terms, whose effects of our simulations and the obtained results are studied and discussed.

Nowadays, numerical simulations play a complementary role to observations in exploration of the solar atmosphere and in particular in understanding the propagation of waves and their contribution to the chromospheric and coronal heating. In this context, [Khomenko & Collados \(2012\)](#) studied the heating of the solar chromosphere resulting from ion-neutral collisions, referred to as ambipolar diffusion. The authors concluded that ambipolar diffusion has the potential to efficiently heat the chromosphere. Additionally, [Kuźma et al. \(2019\)](#), [Niedziela et al. \(2021\)](#), and [Pelekhata et al. \(2021\)](#) showed that in the regime of two-fluid, respectively monochromatic acoustic, impulsively generated magneto-acoustic and Alfvén waves are likely to effectively heat the chromosphere. Moreover, [Srivastava et al. \(2018\)](#) proposed that the small-scale, two-fluid penumbral jets that are omnipresent in active regions, possess sufficient energy to heat the solar corona. In other papers, [Wójcik et al. \(2018, 2019b\)](#) confirmed that ion-neutral collisions result in thermal energy release ([Carlsson et al. 2019](#); [Martínez-Sykora et al. 2020a](#)). [Maneva et al. \(2017\)](#) demonstrated that two-fluid ion magneto-acoustic-gravity waves locally heat solar magnetic flux-tubes. [Wójcik et al. \(2020\)](#) and [Murawski et al. \(2020\)](#) performed respectively 2D and 3D radiative numerical simulations of granulation generated two-fluid waves that effectively heat the plasma, compensating for the radiative energy losses. [Wójcik et al. \(2019a\)](#) showed that granulation-generated jets and associated plasma outflows may contribute to the origin of the fast component of the solar wind ([Tian et al. 2014](#)). There are also recent studies that associate the network jets with propagating heating events and not strong flows (e.g., [De Pontieu et al. 2017](#)).

Despite the above studies, which addressed some parts of the localized heating problem, a full treatment of the energy flow from the deeper and cooler to the outer and hot solar atmospheric layers still remains unsolved. Yet, such full treatment including all these layers is necessary in order to solve this heating problem in the solar chromosphere. Therefore, this paper is devoted to such

a general approach in which the problem is addressed by studying the propagation and dissipation of granulation generated waves and plasma flows in a self-consistent way. More specifically, the earlier two-fluid models of [Wójcik et al. \(2020, 2019a,b\)](#) and [Murawski et al. \(2020\)](#) are generalized by considering all non-adiabatic and non-ideal effects as well as ionization and recombination within the two-fluid model of the solar atmosphere, which takes into account collisions between protons+electrons and neutrals (hydrogen atoms). The following section presents a detailed description of the model. Sections 3 and 4 contain the numerical results and the conclusions, respectively.

2 Physical model and governing equations

Consider the solar atmosphere as a system consisting of interacting fluids: ions (protons+electrons) and hydrogen atoms, denoted respectively by subscripts i and n . Each fluid is characterized by its number density n_k , $k = \{i, n\}$, mass density $\varrho_k = n_k m_k$ with mass m_k , velocity \mathbf{V}_k , gas pressure p_k , and temperature T_k . These fluids are described by the following equations (e.g., [Khomenko & Collados 2012](#); [Leake et al. 2014](#); [Maneva et al. 2017](#); [Meier & Shumlak 2012](#); [Oliver et al. 2016](#); [Popescu Braileanu et al. 2019](#); [Zaqarashvili et al. 2011](#)):

$$\frac{\partial \varrho_i}{\partial t} + \nabla \cdot (\varrho_i \mathbf{V}_i) = m_i (\Gamma_i^{\text{ion}} + \Gamma_i^{\text{rec}}), \quad (1)$$

$$\frac{\partial \varrho_n}{\partial t} + \nabla \cdot (\varrho_n \mathbf{V}_n) = m_n (\Gamma_n^{\text{ion}} + \Gamma_n^{\text{rec}}), \quad (2)$$

$$\frac{\partial (\varrho_i \mathbf{V}_i)}{\partial t} + \nabla \cdot (\varrho_i \mathbf{V}_i \mathbf{V}_i + p_i \mathbf{I}) = \varrho_i \mathbf{g} + \frac{1}{\mu} (\nabla \times \mathbf{B}) \times \mathbf{B} + \nabla \cdot \mathbf{\Pi}_i + \mathbf{S}_i, \quad (3)$$

$$\frac{\partial (\varrho_n \mathbf{V}_n)}{\partial t} + \nabla \cdot (\varrho_n \mathbf{V}_n \mathbf{V}_n + p_n \mathbf{I}) = \varrho_n \mathbf{g} + \nabla \cdot \mathbf{\Pi}_n + \mathbf{S}_n, \quad (4)$$

$$\begin{aligned} \frac{\partial E_i}{\partial t} + \nabla \cdot \left[\left(E_i + p_i + \frac{\mathbf{B}^2}{2\mu} \right) \mathbf{V}_i - \frac{\mathbf{B}}{\mu} (\mathbf{V}_i \cdot \mathbf{B}) \right] + \\ \nabla \cdot \left[\frac{\eta}{\mu} (\nabla \times \mathbf{B}) \times \mathbf{B} \right] = (\varrho_i \mathbf{g} + \mathbf{S}_i) \cdot \mathbf{V}_i + Q_i + \\ \nabla \cdot (\mathbf{V}_i \cdot \mathbf{\Pi}_i) + \nabla \cdot \mathbf{q}_i - L_r^i + H_r, \quad (5) \end{aligned}$$

$$\begin{aligned} \frac{\partial E_n}{\partial t} + \nabla \cdot [(E_n + p_n) \mathbf{V}_n] = (\varrho_n \mathbf{g} + \mathbf{S}_n) \cdot \mathbf{V}_n + Q_n + \\ \nabla \cdot (\mathbf{V}_n \cdot \mathbf{\Pi}_n) + \nabla \cdot \mathbf{q}_n - L_r^n, \quad (6) \end{aligned}$$

$$E_i = \frac{\varrho_i \mathbf{V}_i^2}{2} + \frac{p_i}{\gamma - 1} + \frac{\mathbf{B}^2}{2\mu}, \quad (7)$$

$$E_n = \frac{\varrho_n \mathbf{V}_n^2}{2} + \frac{p_n}{\gamma - 1}, \quad (8)$$

$$\frac{\partial \mathbf{B}}{\partial t} = \nabla \times (\mathbf{V}_i \times \mathbf{B} - \eta \nabla \times \mathbf{B}), \quad \nabla \cdot \mathbf{B} = 0. \quad (9)$$

Here, the reaction rates of the electron impact ionization and radiative recombination, $\Gamma_{i,n}^{\text{ion,rec}}$, momentum collisional, $\mathbf{S}_{i,n}$, and energy source, $Q_{i,n}$, terms are defined as

$$\Gamma_i^{\text{ion}} = -\Gamma_n^{\text{ion}} = n_n \nu^{\text{ion}}, \quad \Gamma_n^{\text{rec}} = -\Gamma_i^{\text{rec}} = n_i \nu^{\text{rec}}, \quad (10)$$

$$\mathbf{S}_i = \mathbf{R}_i^{\text{in}} + \Gamma_i^{\text{ion}} m_i \mathbf{V}_n - \Gamma_n^{\text{rec}} m_i \mathbf{V}_i, \quad (11)$$

$$\mathbf{S}_n = -\mathbf{R}_i^{\text{in}} + \mathbf{R}_n^{\text{ne}} - \Gamma_i^{\text{ion}} m_i \mathbf{V}_n + \Gamma_n^{\text{rec}} m_i \mathbf{V}_i, \quad (12)$$

$$\mathbf{R}_k^{\text{kl}} = \varrho_k \nu_{kl} (\mathbf{V}_l - \mathbf{V}_k), \quad k, l = \{i, n\}, \quad l \neq k, \quad (13)$$

$$Q_i = \frac{1}{2} m_i (\Gamma_i^{\text{ion}} V_n^2 - \Gamma_i^{\text{rec}} V_i^2) + \frac{m_i}{m_n} Q_n^{\text{ion}} - Q_i^{\text{rec}} + Q_i^{\text{in}}, \quad (14)$$

$$Q_n = \frac{1}{2} m_i (\Gamma_n^{\text{rec}} V_i^2 - \Gamma_n^{\text{ion}} V_n^2) + Q_i^{\text{rec}} - Q_n^{\text{ion}} + Q_n^{\text{ni}} \quad (15)$$

with the chemical reactions,

$$Q_n^{\text{ion}} = \frac{3}{2} \Gamma_i^{\text{ion}} k_B T_n, \quad Q_i^{\text{rec}} = \frac{3}{2} \Gamma_n^{\text{rec}} k_B T_i, \quad (16)$$

and the collisional energy exchange terms (Draine 1986),

$$Q_k^{\text{kl}} = \frac{1}{2} \nu_{kl} \varrho_k (\mathbf{V}_k - \mathbf{V}_l)^2 + \frac{3}{2} \frac{k_B \nu_{kl} \varrho_k}{m_k + m_l} (T_l - T_k), \quad k, l = \{i, n\}, \quad l \neq k. \quad (17)$$

In the above equations, $\mathbf{g} = [0, -g, 0]$ denotes the gravity with $g = 274.78 \text{ m s}^{-2}$, \mathbf{B} is the magnetic field and μ is the magnetic permeability of the medium.

The viscous stress tensor is given as (Braginskii 1965)

$$\mathbf{\Pi}_{i,n} = \nu_{1i,n} [\nabla \mathbf{V}_{i,n} + (\nabla \mathbf{V}_{i,n})^T] + \left(\nu_{2i,n} - \frac{2}{3} \nu_{1i,n} \right) \nabla \cdot \mathbf{V}_{i,n} \quad (18)$$

with coefficients $\nu_{1i,n}$ and $\nu_{2i,n}$ being the first (shear) and second (bulk) parameter of viscosity, respectively. Here one follows Hollweg (1986) and takes

$$\nu_{1i,n} = 10^{-16} T_{i,n}^{5/2} \text{ g cm}^{-1} \text{ s}^{-1}. \quad (19)$$

Additionally, for simplicity reasons $\nu_{2i,n} = 0$ is set.

6 *Solar chromospheric heating and plasma outflows*

The magnetic resistivity coefficient, η , is taken in its simplified form as (Ballester et al. 2018)

$$\eta = \frac{\varrho_i \nu_{ei} + \varrho_n \nu_{en}}{e^2 n_e^2}, \quad (20)$$

where ν_{en} and ν_{ei} are respectively the electron-neutral and electron-ion collisions frequencies.

The collision frequency between protons+electrons and hydrogen atoms is specified as (Ballester et al. 2018; Braginskii 1965; Goodman 2004; Khomenko & Collados 2012)

$$\nu_{kl} = \frac{4}{3} \frac{\sigma_{kl} \varrho_l}{m_k + m_l} \sqrt{\frac{8k_B}{\pi} \left(\frac{T_k}{m_k} + \frac{T_l}{m_l} \right)}, \quad k, l = \{i, n\}, \quad l \neq k \quad (21)$$

with $\sigma_{kl} = \sigma_{lk}$ being the collisional cross-section for k- and l-species for which its classical values of $\sigma_{in} = \sigma_{ei} = 1.4 \times 10^{-19} \text{ m}^2$ and $\sigma_{en} = 2 \times 10^{-19} \text{ m}^2$ are chosen from Vranjes & Krstic (2013). See Wargnier et al. (2022) for recently derived expressions for collision frequencies.

The temperatures are given by the ideal gas laws,

$$p_k = \frac{k_B}{m_k} \varrho_k T_k, \quad k = \{i, n\}, \quad (22)$$

with the k-specie gas pressure p_k and mass m_k , k_B is the Boltzmann constant, and $\gamma = 5/3$ is the specific heats ratio.

In Eq. (10) the symbols ν^{ion} and ν^{rec} denote the ionization and recombination frequencies, i.e. (Ballai 2019; Popescu Braileanu et al. 2019; Smirnov 2003; Snow & Hillier 2021; Voronov 1997):

$$\nu^{\text{ion}} \approx n_e A \frac{1}{X + \phi_i/T_e^*} \left(\frac{\phi_i}{T_e} \right)^K \exp \left\{ - \left(\frac{\phi_i}{T_e} \right) \right\}, \quad (23)$$

$$\nu^{\text{rec}} \approx 2.6 \times 10^{-19} \times \frac{n_e}{\sqrt{T_e^*}}, \quad (24)$$

with $\phi_i = 13.6 \text{ eV}$, n_e electron particle density, T_e^* electron temperature expressed in eV, $A = 2.91 \times 10^{-14}$, $K = 0.39$ and $X = 0.232$. According to Carlsson & Leenaarts (2012) radiative recombination may be important in the chromosphere and in the low corona. Note that an advanced multi-fluid model of the solar atmosphere was recently developed by Martínez-Sykora et al. (2020b) which is also capable of treating nonequilibrium ionization, radiation, thermal conduction, and other complex processes in the solar atmosphere.

The radiative loss terms, $L_r^{i,n}$, are implemented: (a) in the photosphere and in the low chromosphere in the framework of thick radiation for protons+electrons and neutrals, described in details by Abbett & Fisher (2012) and (b) in the higher atmospheric layers as thin radiation for ions (Moore & Fung 1972). Note that radiation for neutrals is neglected in high atmosphere

due to low mass density of neutrals there. The thick radiation for ions and neutrals are conditionally implemented in the solar atmosphere, for $y \geq 0$ Mm and for $0.1 < \tau < 10$, where τ is optical distance (e.g., [Abbett & Fisher 2012](#)). Otherwise, in the top chromosphere and in the solar corona, for $\tau \leq 0.1$, thin cooling is adopted for ions.

The symbols $\mathbf{q}_{i,n}$ denote thermal conduction fluxes. For neutrals thermal conduction flux is isotropic and expressed by the following formula:

$$\mathbf{q}_n = \kappa_n \nabla T_n. \quad (25)$$

Here the conduction coefficient is given as ([Cranmer et al. 2007](#))

$$\kappa_n = \frac{29.6 T_n}{1 + \sqrt{7.6 \cdot 10^5 \text{ K}/T_n}} \frac{m_n}{k_B}, \quad (26)$$

where $k_B = 1.3807 \cdot 10^{-16} \text{ cm}^2 \text{ g s}^{-2} \text{ K}^{-1}$ is the Boltzmann constant. Thermal conduction for ions is strongly anisotropic with thermal conduction across magnetic field lines being negligibly small. Therefore, it is assumed that the thermal conduction operates along magnetic field lines, and the flux is described as follows:

$$\mathbf{q}_i = \kappa_{\parallel} \mathbf{b} \nabla (\mathbf{b} \cdot T_i), \quad (27)$$

with $\mathbf{b} = \mathbf{B}/B$ being a unit vector along magnetic field. The parallel thermal conduction coefficient, κ_{\parallel} , is taken from [Spitzer \(1962\)](#) as

$$\kappa_{\parallel} \approx 4.6 \cdot 10^{13} \left(\frac{T_e}{10^8 \text{ K}} \right)^{5/2} \frac{40}{\Lambda} \text{ erg s}^{-1} \text{ cm}^{-1} \text{ K}^{-1} \quad (28)$$

with the quantum Coulomb logarithm ([Honda 2013](#))

$$\Lambda \approx 30.9 - \log \frac{n_e^{1/2}}{T_e k_B^*}. \quad (29)$$

Here k_B^* is the Boltzmann constant expressed in eV K^{-1} .

In Eq. (5) the heating term, H_r , is optionally set. The source of this term could be associated with high-frequency ion-cyclotron waves that operate in the upper parts of the solar atmosphere ([Squire et al. 2022](#)), torsional Alfvén waves ([Finley et al. 2022](#)) or with any other heating process (e.g., [De Pontieu et al. 2022](#)). The following cases are considered here: (a) no heating with $H_r = 0$; (b) heating with $H_r = -L_r$. Hence, the heating term, if adopted, balances the thin radiation and it is implied in all regions in which ion temperature is higher than $15 \cdot 10^3 \text{ K}$. This value of the ion temperature corresponds to the low corona, and it has been chosen somehow arbitrary. In future studies, more realistic heating terms may be adopted such as, for instance, the recently used heating term which could be parameterised by a power-law function of

the local plasma conditions, $H_r \sim \varrho_i^a T_i^b$, where a and b are treated as free parameters (Kolotkov & Nakariakov 2022).

To avoid the generation of transients, all non-adiabatic and non-ideal terms are ramped by setting them equal to 0 at $t = 0$ s and then they are allowed to linearly grow in time until $t = 10^3$ s. Later, they are kept equal to their physical values. The selenoidal condition of Eq. (9) is controlled by a hyperbolic divergence-cleaning technique of Dedner et al. (2002). A second-order spatially accurate Godunov-type method with HLLD Riemann solver (Miyoshi & Kusano 2005) and third-order Runge-Kutta method (Durran 2010) for integration in time with the Courant-Friedrichs-Lewy number equal to 0.9 are used. All non-ideal and non-adiabatic terms in the two-fluid equations are treated implicitly in a separate step using operator splitting with Super-Time-Stepping technique (Alexiades et al. 1996).

Note that in the limit of long wavelength/period waves, the two-fluid equations approach the two-species equations. In this limit $\mathbf{V}_i \approx \mathbf{V}_n$, and one momentum equation together with two mass conservation equations are required; e.g., one mass conservation equation for ϱ_i and another one for $\varrho_i + \varrho_n$. Such a set of equations is called the two-species equations which are widely used in space weather (e.g. Ma et al. 2013; Shou et al. 2016; Tanaka & Murawski 1997; Terada et al. 2009, and references therein). MHD equations would result from the two-species equations for $\varrho_n = 0$, corresponding to a fully-ionized medium. Consequently, a two-fluid model exhibits a potential implication in the given scientific context, even if it is run for long wavelength/period waves. Moreover, a two-fluid model is superior over an MHD model with ambipolar diffusion, as the former provides information about dynamics of neutrals, while the latter suffers from the lack of it. We do not discuss dynamics of neutrals in this paper, however. We focus on evolution of ions and in particular on their temperature, vertical velocities and wave-periods of the excited ion waves, instead. These ion properties consist a set of solar observables, while observational techniques for neutrals require further developments (Khomenko et al. 2016). However, see Zapiór et al. (2022) for the recent report on ion-neutral velocity drift observed in a solar prominence.

3 Computational Results

3.1 Numerical model and solar atmosphere structure

The 2.5D numerical simulations of wave propagation and dissipation in the solar atmosphere are performed with the JOANNA code (Wójcik et al. 2020, 2019a,b), which solves the non-ideal and non-adiabatic two-fluid equations within a simulation box that is specified along the horizontal (x -) and vertical (y -) directions as $(-10.24 \leq x \leq 10.24)$ Mm \times $(-5.12 \leq y \leq 40)$ Mm. The system is assumed invariant along the z -direction (i.e. $\partial/\partial z = 0$). Below the level $y = 5.12$ Mm, a uniform grid with cell size 20 km \times 20 km is set, while higher up the grid is stretched along the y -direction, dividing it into 64 cells whose sizes steadily grow with height. The stretched grid size, Δy_j , is specified

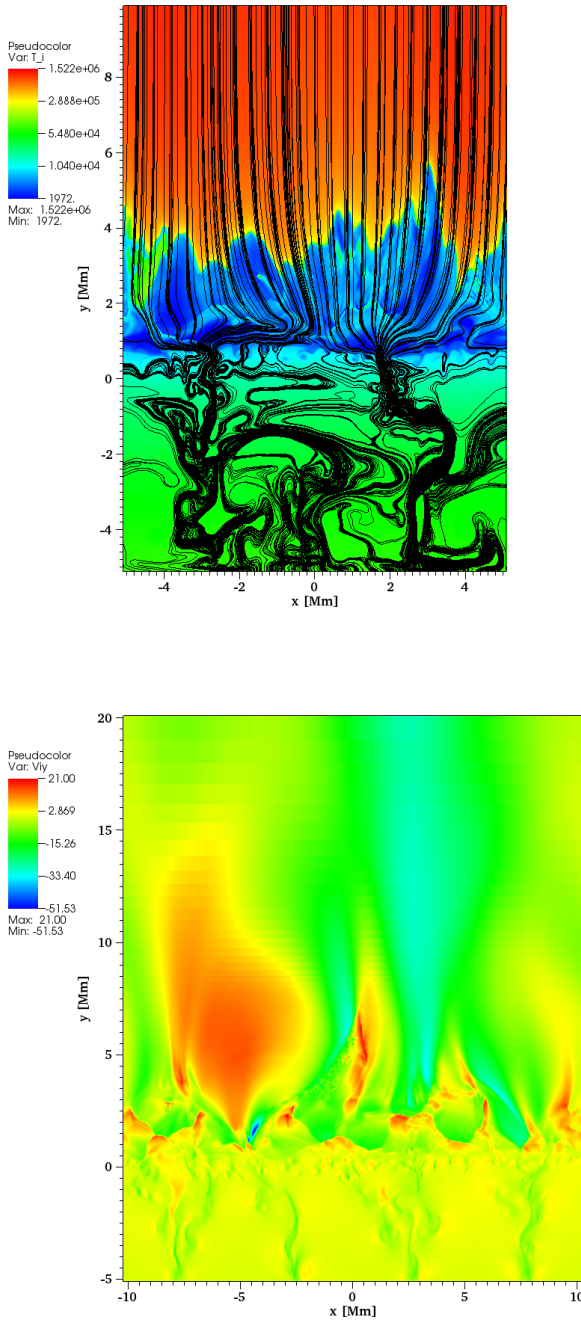


Fig. 1 Spatial profiles of $\log T_i$, overlaid by magnetic field lines (top) and the vertical component of the ion velocity V_{iy} (bottom) for $H_r = 0$. The profiles for $H_r = -L_r$ look qualitatively similar (not shown). The ion temperature, T_i , and vertical component of ion velocity, are expressed in Kelvin and km s^{-1} , respectively.

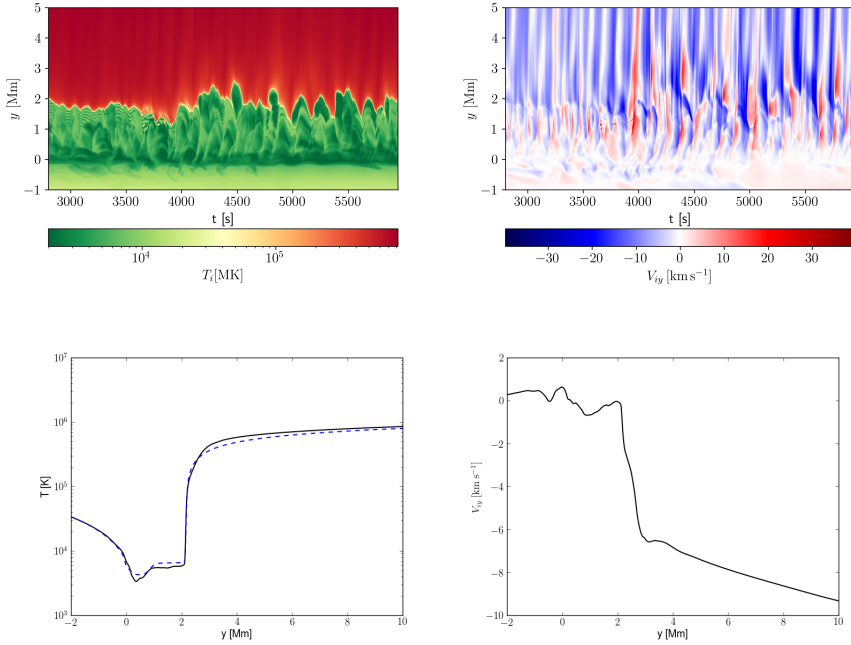


Fig. 2 Top: Time-distance plots for the ion temperature (left) and the vertical component of the ion velocity (right), evaluated at $x = 0$. Bottom: Temporally averaged ion temperature (left: solid line), semi-empirical data of Avrett & Loeser (2008) (left: dashed line) and vertical component of the ion velocity (right) vs height y for the case of $H_r = 0$.

as

$$\Delta y_j = r^j \Delta y, \quad j = 1, 2, \dots, 64, \quad (30)$$

where $\Delta y = 20$ km is the uniform grid size and the stretching ratio r is given as

$$y_t - y_b = \sum_{j=1}^{j=64} \Delta y_j. \quad (31)$$

Here, $y_b = 5.12$ Mm and $y_t = 40$ Mm are the bottom-most and top-most points of the stretched grid zone.

At $y = -5.12$ Mm and at $y = 40$ Mm all plasma quantities are fixed to their magnetostatic values at all times $t \geq 0$ s. The left and right boundary conditions are set to be periodic. Our simulations are initiated at $t = 0$ s by implementing a hydrostatic solar atmosphere with the semi-empirical temperature profile, $T(y)$, according to the model of Avrett & Loeser (2008). This temperature, which initially (at $t = 0$ s) is identical for ions and neutrals, $T_i(x, y, t = 0) = T_n(x, y, t = 0) = T(y)$, uniquely determines the equilibrium ion and neutral mass densities and gas pressures (e.g. Murawski et al. 2020). Then, convective instabilities occur in the system self-consistently. These instabilities are most prominent below the photosphere, and they lead

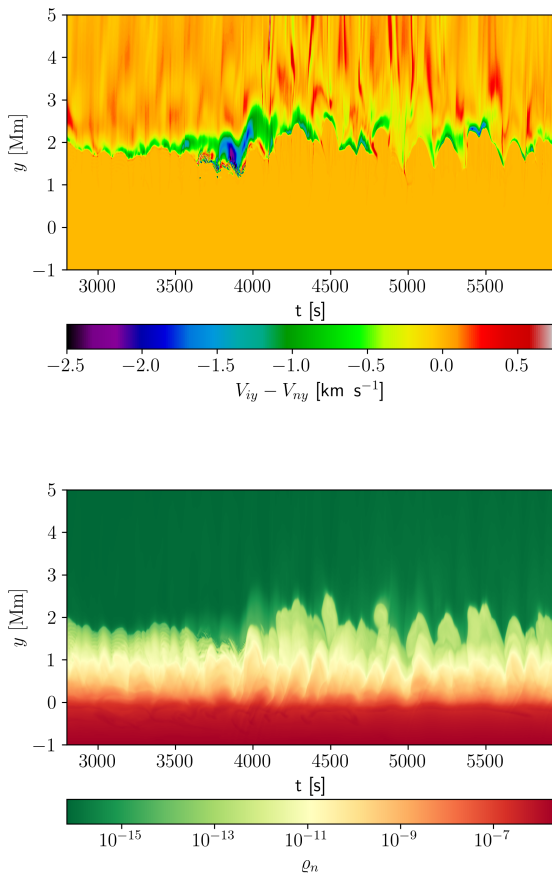


Fig. 3 Time-distance plot for the horizontally averaged ion and neutral vertical components of velocity drift, $V_{iy} - V_{ny}$, (top) and neutral mass density, ρ_n , (bottom) for $H_r = -L_r$.

to self-generated and self-evolving turbulent fields that mimic the convection with granulation cells at its top (Fig. 1, top). Such turbulent fields reshape the initial magnetic field, which is taken in the form of the four arcades, given as

$$B_x = B_0 \cos\left(\frac{x}{\Lambda_B}\right) \exp\left(-\frac{y}{\Lambda_B}\right), \quad (32)$$

$$B_y = -B_0 \sin\left(\frac{x}{\Lambda_B}\right) \exp\left(-\frac{y}{\Lambda_B}\right), \quad (33)$$

with $B_0 = 20$ Gs, $\Lambda_B = 2L/\pi$ and $L = 2.56$ Mm, being overlaid by the straight magnetic field $[B_x, B_y, B_z] = [0, 10, 2]$ G. This initial magnetic field evolves into well developed complex structures below the transition region (Fig. 1,

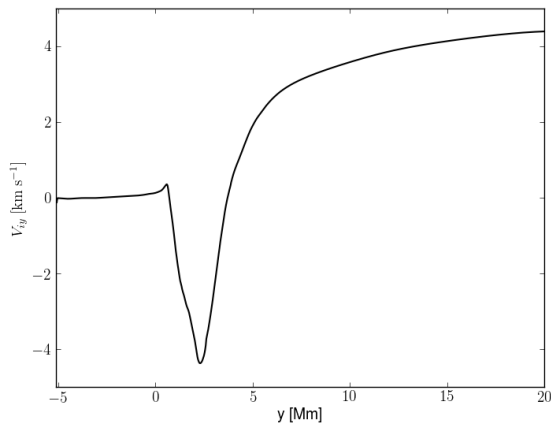


Fig. 4 Horizontally and temporally averaged vertical component of the ion velocity vs height y for the case of $H_r = -L_r$.

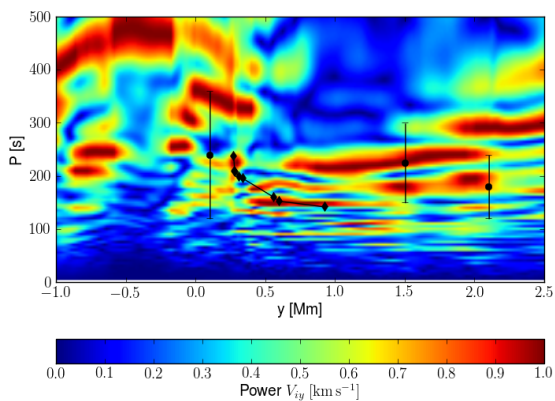


Fig. 5 Wave periods, P , evaluated from the Fourier power spectrum for the ion vertical velocity of Fig. 2 (right-top) (contour plots). The diamonds and dots show the observational data obtained by [Wiśniewska et al. \(2016\)](#) and [Kayshap et al. \(2018\)](#), respectively.

top). The spatial profile of $\log T_1(x, y)$ exhibits a perturbed pattern that shows oscillations and jets in the transition region, which was initially located at the level of $y = 2.1$ Mm, as can be seen in the profile of $T(y)$ (Fig. 2, left-bottom, dashed line). The granulation-generated jets are well seen in the spatial profile of $\log T_1(x, y)$; the largest jet is located at $x \approx 0.5$ Mm and it reaches the height of $y \approx 6$ Mm (Fig. 1, top).

Figure 2 (left-top) shows the ion temperature, evaluated at $x = 0$ Mm. In general, its averaged-over-time quantity exhibits a similar distribution as

the atmospheric temperature in the semi-empirical model of [Avrett & Loeser \(2008\)](#) (Fig. 2, left-bottom).

3.2 Waves and dynamics of fluid species

3.2.1 Chromospheric heating

The self-generated granulation, which is responsible for the wave generation, also expels cold ions and neutrals from the lower atmospheric layers into the transition region and low corona. As a result, the transition region is shifted, which triggers plasma flows in the background atmosphere because the whole system is perturbed. The expelled ions reach their maximum velocities of $V_{iy} \approx 21 \text{ km s}^{-1}$ (Fig. 1, bottom), and they are heated by ion-neutral collisions, which is an important signature in the context of chromospheric heating. As a result of ion-neutral collisions, the energy of these excited waves is dissipated. This dissipation is most effective for largest dispatches between ion and neutral velocities, and these waves may convert their energy into heat mostly in the chromosphere, compensating radiative and thermal losses. Indeed, the vertical component of the ion-neutral velocity drift, $V_{iy} - V_{ny}$, attains largest values at the transition region and in the low corona (Fig. 3, top), leading to collisional heating there ([Martínez-Sykora et al. 2020b](#)).

In the solar photosphere, collisions between neutrals and ions are frequent, and yet, wave damping is not significant because of the high frequency of collisions that equalize momenta of neutrals and ions quickly. On the other hand, in the solar chromosphere the collisions are less frequent and, as a result, there are differences in momenta between neutrals and ions, which makes the damping of flows and short-wavelength waves more effective. Our results also demonstrate that neutrals that reach the lower layers of the solar corona undergo ionization. The presence of such neutrals in the lower corona is responsible for damping of flows and waves that carry their energy up to these layers. However, the efficiency of wave damping in the corona is not high, therefore, the dissipated wave energy is not sufficient to balance the observed radiative losses ([Squire et al. 2022](#)). To account for these differences, an extra energy term is included in our numerical model (see Section 2), and the effects of this term are presented and discussed below.

3.2.2 Dynamics of neutrals

The obtained results show that our two-fluid model reveals dynamics of neutrals, which play an important role in the layers of the solar atmosphere that are simulated in this paper. Figure 3 (bottom) illustrates the time-distance plot of neutral mass density, ρ_n , collected at $x = 0 \text{ Mm}$. The pattern of oscillations seen in this figure at the transition region, $y = 2.1 \text{ Mm}$, is prominent and it demonstrates the role played by neutrals in the physical processes of the solar atmosphere. This role can only be investigated by the two-fluid model presented in this paper; note that no model based on MHD with ambipolar diffusion would give any description of the dynamics of neutrals.

3.2.3 Plasma flows

The second central issue of the solar physics research that is addressed in the present paper concerns the origin of the solar wind. In the magnetic-free, terrestrial atmosphere the wind blows from the high-pressure regions to the low-pressure weather systems. However, with the solar corona being permeated by magnetic fields, the nascent fast wind originates from the magnetic network (Hassler et al. 1999). Moreover, Tu et al. (2005) and Tian et al. (2010) proposed that the wind starts in coronal funnels at altitudes in between 5 to 20 Mm above the photosphere, and Dadashi et al. (2011) reported average plasma upflows of (-1.8 ± 0.6) km s⁻¹ at 1 MK temperature.

From Fig. 1 (bottom) it follows that the (red) patches of $\simeq 20$ km s⁻¹ of the ion outflows, V_{iy} , are located at several points in the corona. The downfalls of $\simeq -50$ km s⁻¹ with the gravitationally attracted plasma is also clearly seen at a few locations. However, it is important that vertical component of ion velocity evaluated at $x = 0$ Mm exhibits quasi-periodic upflows and downfalls that are discernible at various moments in time, e.g. at $t = 4 \cdot 10^3$ s with $\max(V_{iy}) \simeq 45$ km s⁻¹ (Fig. 2, right-top), and the vertical component of ion velocity averaged over time reveals downfalls of its magnitude growing with height (Fig. 2, right-bottom). These flows seem to share several properties of type I spicules (see, e.g., Draine 1986; Hansteen et al. 2006; Sterling 2000; Tsiropoula et al. 2012). Note that there is some previous work on the velocity average across the solar atmosphere, and that the atmospheric heating occurs naturally even within the framework of a single-fluid MHD model (e.g., Hansteen et al. 2010). The two-fluid model presented in this paper and the obtained results significantly generalize the previous work by allowing to describe dynamics of neutrals and ions, and their role in the solar atmosphere heating.

The upflows seen in the simulation are more relevant to regions of the quiet Sun with a vertical orientation of the magnetic field. Downflows are observed at the sides of the funnels with, obviously, oblique magnetic field. Regions of the quiet Sun with a horizontally oriented magnetic field do not exhibit that many upflows (Fig. 1, bottom).

In a quiet region, the plasma downfalls of the maximum magnitude of $5 - 10$ km s⁻¹ and averaged upflows of about 2 km s⁻¹ were recently reported by Kayshap et al. (2015) and Tian et al. (2021). The results of Figs. 1 (bottom) and 2 (right), demonstrate that the plasma upflows (Fig. 4) originate from the granulation-generated jets between $y = 4$ Mm and $y = 20$ Mm, which is consistent with the data reported by Tian et al. (2010). Our numerical simulations show that such upflows are generated when the extra heating term in the energy equation is taken into account (see Section 2) to balance the radiative losses from the optically thin solar corona with the ion temperature $T_i > 15 \cdot 10^3$ K ($H_r = -L_r$).

It must be pointed out that without the heating term ($H_r = 0$) only downward plasma flows result from our numerical simulations. Let us remark

that the added heating term mimics coronal plasma heating by high-frequency ion-cyclotron waves as recently proposed by [Squire et al. \(2022\)](#).

3.3 Wave cutoffs and their observational verification

Wave cutoffs arises naturally in stratified media with nonuniform magnetic fields, and they can be used to determine ranges of frequencies corresponding to propagating or evanescent waves. The cutoff is used to establish the ranges of periods for the propagating and reflected waves in the solar atmosphere. For the recent discussion see e.g. [Routh et al. \(2020\)](#). Specifically, the role of the acoustic cutoff in the solar atmosphere has been extensively studied and different formulas for this cutoff are summarized by [Wiśniewska et al. \(2016\)](#), who showed that none of those formulas could reproduce their observational results. The observational results presented by [Wiśniewska et al. \(2016\)](#) and [Kayshap et al. \(2018\)](#) demonstrated variations of the cutoff in the upper photosphere, lower chromosphere, and in the transition region. There have been attempts to account numerically for the observed variations of the acoustic cutoffs (e.g. [Murawski & Musielak 2016](#); [Murawski et al. 2016](#)) but only partial agreement was found. Therefore, in this paper, we compute variations of the acoustic cutoff in the considered layers of the solar atmosphere and compare our numerical results to the observational data reported by [Wiśniewska et al. \(2016\)](#) and [Kayshap et al. \(2018\)](#).

Figure 5 illustrates wave periods (contour plots) obtained from the Fourier power spectrum of $V_{iy}(x = 0, y, t)$, illustrated in Fig. 2 (right-top). These wave periods are compared to the observational data analyzed by [Wiśniewska et al. \(2016\)](#) and [Kayshap et al. \(2018\)](#). This figure displays a multitude of wave power concentrations at different periods and heights, but a few of them correspond approximately to the location of the wave power concentrations found in the observational data. Nevertheless, the agreement between our numerical results and the data presented in the above figure confirms that ion-neutral collisions are efficient energy release processes, resulting in kinetic energy dissipation and its conversion into heat.

It must be also noted that there have been done studies of cutoffs of two-fluid waves in atmospheric models that have ion-neutral interactions included (see references in [Alharbi et al. 2022](#); [Ballester et al. 2018](#)). For instance, slow magneto-acoustic waves arise for sufficient short wavelengths only, and for long wavelengths these waves have only imaginary frequencies which correspond to non-oscillatory damping (see Fig. 3 in [Zaqarashvili et al. 2011](#)). Similarly, according to [Soler et al. \(2013\)](#) Alfvén waves of a given frequency are not propagating within a certain range of their wavelengths.

4 Conclusions and summary

Numerical simulations of two-fluid waves and plasma flows were performed in a partially ionized quiet-Sun region, taking into account non-adiabatic and non-ideal effects with ionization and recombination included self-consistently

into the model (Ballester et al. 2018). The considered neutral acoustic-gravity and ion Alfvén and magneto-acoustic-gravity waves were generated by spontaneously evolving and self-organizing convection. For the recent analysis of acoustic-gravity wave propagation in 3D radiation hydrodynamic numerical simulations of the solar atmosphere see Fleck et al. (2021). The energy carried by the excited non-potential magnetic field, sheared plasma flows, and waves is dissipated by ion-neutral collisions and non-ideal (magnetic diffusivity and viscosity) effects, effectively heating the plasma and compensating radiative and thermal energy losses. This dissipation leads to local heating of the background chromosphere. In comparison to the previous study by Martínez-Sykora et al. (2017), Fleck et al. (2021), Snow & Hillier (2021), and Navarro et al. (2022), who adopted complex non-adiabatic MHD models, for a partially-ionized plasma, and Wójcik et al. (2020) and Murawski et al. (2020), who used a two-fluid numerical model including radiation, our results show that taking into account radiation, anisotropic thermal conduction, magnetic diffusivity, viscosity, ionization and recombination (Ballester et al. 2018) leads to a solar atmosphere with a vertical temperature profile that resembles the semi-empirical data of Avrett & Loeser (2008). There were also attempts to assess the efficiency or feasibility of heating by waves by comparing the wave flux with the radiative losses. See e.g. Abbasvand et al. (2020) for the recent studies. Additionally, the obtained results for wave periods show a quantitative agreement with the observational data of Wiśniewska et al. (2016) and Kayshap et al. (2018).

Therefore, we conclude that the granulation-generated two-fluid waves effectively heat the background medium and the simultaneously excited weak plasma outflows exhibit physical parameters that are consistent with the basic observational findings (Dadashi et al. 2011; Hansteen et al. 2010; Tian et al. 2011). To get these plasma outflows an extra heating term is required. The presence of the heating term is evidence that the amount of energy carried by waves is not sufficient to heat the background atmosphere and at the same time initiate plasma outflows. This limitation of the wave theory resulting from our numerical simulations is likely caused by the lack of momentum deposition by Alfvén waves, whose presence in the solar corona is strongly confirmed by observations. The heating term may actually mimic coronal heating by high-frequency ion-cyclotron waves, which was recently proposed by Squire et al. (2022); however, it must be kept in mind that no plasma waves are considered in our numerical model. Let us also point out that the presence of these outflows may be responsible for the origin of the solar wind.

To briefly summarize our work: the considered numerical model and the presented results contribute to the studies of the required chromospheric heating and, in the case of heating fully balancing the thin cooling for $T > 15 \cdot 10^3$ K, the origin of the fast component of the solar wind. Our present model elucidates a general and global physical picture of the granulation-generated wave motions, plasma flows, and subsequent heating in the non-ideal quiet-Sun

atmosphere. The improved observational estimations on such dynamical phenomena with ultra-high resolution telescopes (e.g., the 4m-DKIST and the upcoming 4m-EST) may further put forward more refinement on such studies in the forthcoming time and, hence, reveal mass and energy transport processes.

Acknowledgments. K.M. expresses his thanks to Fan Zhang, Teimury Zaqarashvili, Elena Khomenko, Błażej Kuźma, Michaela Brchnelova, Ramon Oliver, Gabor Toth, Takashi Tanaka, Naoki Terada, and Ryoya Sakata for stimulating discussions on the adopted two-fluid model. The JOANNA code was developed by Darek Wójcik with some contribution of Luis Kadowaki and Piotr Wołoszkiewicz. This work was done within the framework of the project from the Polish Science Center (NCN) Grant No. 2020/37/B/ST9/00184. A. K. Srivastava acknowledges the ISRO Project Grant (DS_2B512 13012(2)/26/2022-Sec.2) for the support of his research. We visualize the simulation data using the VisIt software package (Childs et al. 2012). SP acknowledges support from the projects C14/19/089 (C1 project Internal Funds KU Leuven), G.0D07.19N (FWO-Vlaanderen), SIDC Data Exploitation (ESA Prodex-12), and Belpo project B2/191/P1/SWiM.

References

- Abbasvand, V., Sobotka, M., Heinzel, P., et al. 2020, *Astrophys. J.*, 890, 22
- Abbett, W. P. & Fisher, G. H. 2012, *Solar Phys.*, 277, 3
- Alexiades, V., Amiez, G., & Gremaud, P.-A. 1996, *Communications in Numerical Methods in Engineering*, 12, 31
- Alharbi, A., Ballai, I., Fedun, V., & Verth, G. 2022, *MNRAS*, 511, 5274
- Avrett, E. H. & Loeser, R. 2008, *ApJS*, 175, 229
- Ballai, I. 2019, *Frontiers in Astronomy and Space Sciences*, 6, 39
- Ballester, J. L., Alexeev, I., Collados, M., et al. 2018, *Space Science Rev.*, 214, 58
- Biermann, L. 1946, *Naturwissenschaften*, 33, 118
- Braginskii, S. I. 1965, *Reviews of Plasma Physics*, 1, 205
- Carlsson, M., De Pontieu, B., & Hansteen, V. H. 2019, *Ann. Rev. Astron. Astrophys.*, 57, 189
- Carlsson, M. & Leenaarts, J. 2012, *A&A*, 539, A39

- Childs, H., Brugger, E., Whitlock, B., et al. 2012, *VisIt: An End-User Tool For Visualizing and Analyzing Very Large Data* (Chapman and Hall/CRC), 357–372
- Cranmer, S. R., van Ballegoijen, A. A., & Edgar, R. J. 2007, *ApJS*, 171, 520
- Dadashi, N., Teriaca, L., & Solanki, S. K. 2011, *A&A*, 534, A90
- De Moortel, I. & Nakariakov, V. M. 2012, *Philosophical Transactions of the Royal Society of London Series A*, 370, 3193
- De Pontieu, B., Martínez-Sykora, J., & Chintzoglou, G. 2017, *ApJL*, 849, L7
- De Pontieu, B., Testa, P., Martínez-Sykora, J., et al. 2022, *ApJ*, 926, 52
- Dedner, A., Kemm, F., Kröner, D., et al. 2002, *J. Comp. Phys.*, 175, 645
- Draine, B. T. 1986, *MNRAS*, 220, 133
- Durrant, D. R. 2010, *Numerical Methods for Fluid Dynamics*
- Finley, A. J., Brun, S. A., Carlsson, M., et al. 2022, arXiv e-prints, arXiv:2207.02878
- Fleck, B., Carlsson, M., Khomenko, E., et al. 2021, *Philosophical Transactions of the Royal Society of London Series A*, 379, 20200170
- Goodman, M. L. 2004, *A&A*, 416, 1159
- Hansteen, V. H., De Pontieu, B., Rouppe van der Voort, L., van Noort, M., & Carlsson, M. 2006, *ApJL*, 647, L73
- Hansteen, V. H., Hara, H., De Pontieu, B., & Carlsson, M. 2010, *ApJ*, 718, 1070
- Hassler, D. M., Dammasch, I. E., Lemaire, P., et al. 1999, *Science*, 283, 810
- Hegglund, L., Hansteen, V. H., De Pontieu, B., & Carlsson, M. 2011, *ApJ*, 743, 142
- Hollweg, J. V. 1986, *ApJ*, 306, 730
- Honda, M. 2013, *Japanese J. Appl. Phys.*, 52, 108002
- Kayshap, P., Banerjee, D., & Srivastava, A. K. 2015, *Solar Phys.*, 290, 2889
- Kayshap, P., Murawski, K., Srivastava, A. K., Musielak, Z. E., & Dwivedi, B. N. 2018, *MNRAS*, 479, 5512

- Kayshap, P., Srivastava, A. K., Tiwari, S. K., Jelínek, P., & Mathioudakis, M. 2020, *A&A*, 634, A63
- Khomenko, E. & Collados, M. 2012, *ApJ*, 747, 87
- Khomenko, E., Collados, M., & Díaz, A. J. 2016, *ApJ*, 823, 132
- Kolotkov, D. Y. & Nakariakov, V. M. 2022, *Month. Not. Royal Astron.*, 514, L51
- Kuźma, B., Wójcik, D., & Murawski, K. 2019, *ApJ*, 878, 81
- Leake, J. E., DeVore, C. R., Thayer, J. P., et al. 2014, *Space Science Rev.*, 184, 107
- Ma, Y. J., Nagy, A. F., Russell, C. T., et al. 2013, *J. Geophys. Res.*, 118, 321
- Maneva, Y. G., Alvarez Laguna, A., Lani, A., & Poedts, S. 2017, *ApJ*, 836, 197
- Martínez-Sykora, J., De Pontieu, B., Hansteen, V. H., et al. 2017, *Science*, 356, 1269
- Martínez-Sykora, J., Leenaarts, J., De Pontieu, B., et al. 2020a, *ApJ*, 889, 95
- Martínez-Sykora, J., Szydlarski, M., Hansteen, V. H., & De Pontieu, B. 2020b, *ApJ*, 900, 101
- Meier, E. T. & Shumlak, U. 2012, *Physics of Plasmas*, 19, 072508
- Miyoshi, T. & Kusano, K. 2005, *J. Comp. Phys.*, 208, 315
- Moore, R. L. & Fung, P. C. W. 1972, *Solar Phys.*, 23, 78
- Murawski, K. & Musielak, Z. E. 2016, *MNRAS*, 463, 4433
- Murawski, K., Musielak, Z. E., Konkol, P., & Wiśniewska, A. 2016, *ApJ*, 827, 37
- Murawski, K., Musielak, Z. E., & Wójcik, D. 2020, *ApJL*, 896, L1
- Navarro, A., Khomenko, E., Modestov, M., & Vitas, N. 2022, *Astron. Astrophys.*, 663, A96
- Niedziela, R., Murawski, K., & Poedts, S. 2021, *A&A*, 652, A124
- Oliver, R., Soler, R., Terradas, J., & Zaqarashvili, T. V. 2016, *ApJ*, 818, 128
- Pelekhata, M., Murawski, K., & Poedts, S. 2021, *A&A*, 652, A114

- Popescu Braileanu, B., Lukin, V. S., Khomenko, E., & de Vicente, Á. 2019, *A&A*, 627, A25
- Routh, S., Musielak, Z. E., Sundar, M. N., Joshi, S. S., & Charan, S. 2020, *Astron. Space Sc.*, 365, 139
- Schwarzschild, M. 1948, *ApJ*, 107, 1
- Shou, Y., Combi, M., Toth, G., et al. 2016, *ApJ*, 833, 160
- Smirnov, B. M. 2003, *Physics of atoms and ions*, New York: Springer-Verlag, (Graduate texts in contemporary physics)
- Snow, B. & Hillier, A. 2021, *MNRAS*, 506, 1334
- Soler, R., Carbonell, M., Ballester, J. L., & Terradas, J. 2013, *ApJ*, 767, 171
- Spitzer, L. 1962, *Physics of Fully Ionized Gases*, New York: Interscience (2nd edition)
- Squire, J., Meyrand, R., Kunz, M. W., et al. 2022, *Nature Astronomy*, 6, 715
- Srivastava, A. K., Murawski, K., Kuźma, B., et al. 2018, *Nature Astronomy*, 2, 951
- Srivastava, A. K., Shetye, J., Murawski, K., et al. 2017, *Scientific Reports*, 7, 43147
- Sterling, A. C. 2000, *Solar Phys.*, 196, 79
- Tanaka, T. & Murawski, K. 1997, *J. Geophys. Res.*, 102, 19805
- Terada, N., Shinagawa, H., Tanaka, T., Murawski, K., & Terada, K. 2009, *J. Geophys. Res.*, 114, A09208
- Tian, H., DeLuca, E. E., Cranmer, S. R., et al. 2014, *Science*, 346, 1255711
- Tian, H., Harra, L., Baker, D., Brooks, D. H., & Xia, L. 2021, arXiv e-prints, arXiv:2102.02429
- Tian, H., McIntosh, S. W., De Pontieu, B., et al. 2011, *ApJ*, 738, 18
- Tian, H., Tu, C., Marsch, E., He, J., & Kamio, S. 2010, *ApJL*, 709, L88
- Tsiropoula, G., Tziotziou, K., Kontogiannis, I., et al. 2012, *Space Science Rev.*, 169, 181
- Tu, C.-Y., Zhou, C., Marsch, E., et al. 2005, *Science*, 308, 519

- Voronov, G. S. 1997, *Atomic Data and Nuclear Data Tables*, 65, 1
- Vranjes, J. & Krstic, P. S. 2013, *A&A*, 554, A22
- Wang, Y., Yokoyama, T., & Iijima, H. 2021, *ApJL*, 916, L10
- Wargnier, Q. M., Martínez-Sykora, J., Hansteen, V. H., & Pontieu, B. D. 2022, *ApJ*, 933, 205
- Wiśniewska, A., Musielak, Z. E., Staiger, J., & Roth, M. 2016, *ApJ*, 819, L23
- Wójcik, D., Kuźma, B., Murawski, K., & Musielak, Z. E. 2020, *A&A*, 635, A28
- Wójcik, D., Kuźma, B., Murawski, K., & Srivastava, A. K. 2019a, *ApJ*, 884, 127
- Wójcik, D., Murawski, K., & Musielak, Z. E. 2018, *MNRAS*, 481, 262
- Wójcik, D., Murawski, K., & Musielak, Z. E. 2019b, *ApJ*, 882, 32
- Zapiór, M., Heinzl, P., & Khomenko, E. 2022, *The Astrophysical Journal*, 934, 16
- Zaqarashvili, T. V., Khodachenko, M. L., & Rucker, H. O. 2011, *A&A*, 534, A93